

NUMERICAL INTEGRATION EXPERIMENTS WITH VARIABLE-RESOLUTION TWO-DIMENSIONAL CARTESIAN GRIDS USING THE BOX METHOD

WALTER JAMES KOSS

National Hurricane Research Laboratory, Environmental Research Laboratories, NOAA, Miami, Fla.

ABSTRACT

Numerical experiments were performed with variable resolution two-dimensional rectangular Cartesian grids. The shallow-water equations were integrated on several variable-mesh grids and on a constant increment fine-resolution grid; the method of integration used the "box" technique for spatial representation. The grids were designed to be used in numerical experiments that examine vortex-type motions that may be embedded in a fairly uniform basic current. With this in mind, two systems were investigated: (1) a closed system containing a balanced vortex and (2) a semiopen system with east-west cyclic continuity containing a moderately strong easterly jet. The results indicate that, for a weak vortex embedded in a zonal current, a 2-step "telescope"-type grid can be used in numerical integrations with success; that is, the incurred error is relatively small and the computation time and computer memory requirements are not excessive. For an intense vortex, a graded-type grid yields a relatively better numerical integration at the expense of an increase in computation time.

1. INTRODUCTION

Considerable interest has been shown in the use of variable horizontal resolution grids for numerically integrating the equations that govern the behavior of meteorological phenomena. Variable increment-space meshes have been used with some success in studies of models possessing one horizontal space dimension. For two horizontal space-dimensioned models, the interest has been in the embedding of a fine-resolution mesh in a relatively coarse grid to resolve interesting small-scale features that are present in a large-scale environment. In this paper, we are concerned with the characteristics of fine-to-coarse resolution two-dimensional grids which are rectangular Cartesian in nature. These grids are of a type that would be useful in the study of vortex-type motions embedded in a large-scale flow. The integrations make use of a technique that originally appeared in fluid dynamics applications, and that has been given the name "box" method. The method has the desirable property that the momentum and mass of the system are preserved under the finite-difference formulation to within time-differencing errors because the equations are expressed in flux form.

The grid systems described here effect a reduction in the amount of internal storage needed on a computer when compared to a fixed fine-resolution mesh for the same region of integration. Also, computing time is reduced by the elimination of calculation points; but parts of these savings are at the expense of more sophisticated computer programming effort.

One of the advantages of Cartesian systems is the simplicity of the derivatives in both analytic and finite-difference form. This is in comparison with variable grids that are generated by transforming a desired grid structure into a rectangular Cartesian system such as was done by Anthes (1970). Methods of the latter type

increase computation time at each grid point because of the added terms in the tendency equations and introduce transformation factors in the equations that can result in computational difficulties such as those described by Shuman and Stackpole (1968). A further problem with transformation systems is the definition of the boundary when meshing the transformed grid with a large-scale coarse grid. The graded systems described here have a smooth transition into the large-scale system with no additional computations being needed to merge the systems, whereas the non-Cartesian-type grids often incur added computations (and perhaps approximations) where the grids join together. One experiment (No. 18) simulated, to a certain degree, the incorrect handling of the boundary; there, different frequency gravity waves were generated by reflections at the boundary and the effect of their interaction at the center of the vortex was observed.

Truncation error propagation can also be a serious problem. In variable-grid computations (as with computations done on a map-oriented grid), an upper bound on the truncation error is initially given locally by the evaluation of the appropriate series expansion remainder term using the local value of space increment and derivative maximum in this region. If the physical system is principally contained in the fine mesh and does not interact with the environment, the local truncation estimate should hold for the forecast period. Otherwise, system interactions will admit the large-scale truncation into the finer mesh computations; this error will dominate throughout the remainder of the forecast period.

2. GRID STRUCTURE

Three variable-resolution grids and one fixed-resolution grid were used in the numerical integrations. The variable resolution grids were of two basic types: (1) a constant

fine mesh embedded in a constant coarse mesh and (2) a fixed fine mesh embedded in a grid system that becomes progressively coarser with distance from the central region. Both types are members of a generalized family of grids, the construction and characteristics of which are described in the following discussion.¹

The basic construction element of the variable-resolution grids is a square having side length δ . Each graded grid has the following properties:

1. The area elements (boxes) of the grid structure are squares with side lengths that are integral multiples of the basic side length δ .
2. The boxes increase in area outward from the center in a systematic manner.
3. The geometry of contiguous boxes having equal area is that of a "square annulus" (except for the central region).

As will be shown, the square annulus is not necessarily composed of a single ring of boxes.

The above properties set a requirement that contiguous annuli having different area elements must satisfy at their common interface. For definition, consider an inner annulus composed of elements having equal area A_i^2 that is enclosed by an outer annulus with elements having area A_o^2 . Then, if $A_i = n\delta$ and $A_o = n'\delta$, where n and n' are arbitrary positive integers ($n < n'$), the length of a common side, when expressed in terms of the number of boxes in each annulus at the interface, must be an integer relationship. That is,

$$A_i m \equiv (n\delta)m = (n'\delta)m' \equiv A_o m' \quad (1)$$

must hold, where m and m' are positive integers. We will exclude from consideration those cases where n' is an integral multiple of n ; in those cases there is a rapid variation in grid structure that is not acceptable. We wish to construct grids that have a less pronounced variation. The minimal increase in box size is given when $n' = n + 1$. If we begin the construction by having the central "core" region composed of basic area elements only, then the minimal variation requirement allows core regions the sides of which are made up of only even numbers of basic elements. Hence, for i a positive integer, there are $(2i \times 2i)$ elements in the core. Now let $n = 1, 2, \dots$ also represent the count (increasing outward) of the interface between the annuli as defined above. Then the only positive integer solutions at the n th interface for eq (1) above are $m_n = i(n+1)$ and $m'_n = i(n)$. At the $(n+1)$ st interface $m_{n+1} = m'_n + 2i$; from this we see that the index i also represents the number of rings of equal-area boxes which make a square annulus.

The construction for $i=1$, $i=2$, and $i=3$ is shown in figure 1. Here we note how the index i is the controlling factor in the degree of variation possessed by the graded

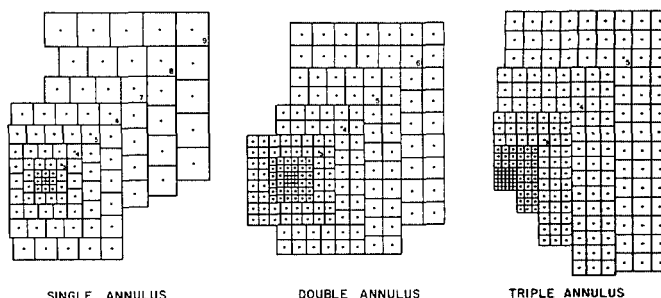


FIGURE 1.—Graded mesh constructions for $i=1$ (single annulus), $i=2$ (double annulus), and $i=3$ (triple annulus). The smallest box in each case has area $=\delta^2$. The number in the box is the value of n [where box area $= (n\delta)^2$] for the "square" annulus which contains the box.

TABLE 1.—Percent increase in box area as a function of n where box area $= (n\delta)^2$

n	1	2	3	4	5	6	7	8	9	10	11	12	13	14
% increase	300	125	77	56	44	36	31	27	23	21	19	17	16	15

mesh and that the grid variation can be reduced by choosing larger values of i , since this essentially introduces regions of constant mesh length throughout the structure. However, for any value of i , the percent increase in box area as a function of n (table 1) is largest for small values of n , which corresponds to the central region of the construction. Since this may not be a desirable feature, modifications to these grids can be made based on the following considerations: (1) the overall scale of the physical system, (2) the scale of the interesting variations within the system, and (3) numerical stability criterion with regard to computational time needed for the integration. All three of these will determine the specification of the magnitude of δ .

The use of a grid devised by the above rules with small values of δ will force the use of small time increments in the numerical integration, which can be economically unfeasible. Also, one desires a variable grid on which the major variations in the physical parameters take place in the fine-resolution portions of the mesh. Hence, item (2) places a restriction on the choice of δ . This, along with item (1), helps determine the grid index i .

Since the percent changes of box area are largest for small values of n and this may be undesirable even in conjunction with large values of the grid variation index i , the central region can be modified by deleting the annuli for small values of $n = 1, 2, \dots, (k-1)$ and replacing the deleted inner region with a fixed-resolution mesh, the boxes of which have side length $k\delta$. This yields a graded grid structure that has a fine resolution inner region and that gradually increases in "mesh length" toward the periphery of the region of interest. The graded grids used here were constructed in this manner. Table 2 gives the

¹ A clarification of nomenclature should be made at this point. Although the words "grid" and "mesh" denote a systematically arranged array of points, we shall use them to denote the "box" structure which is used in the integration technique. In reality a grid or mesh point is a point within a box, that figuratively will be taken as the center of the box.

TABLE 2.—Characteristics of the grid structures used in the numerical experiments. Here, δ^2 is the area of the basic construction element, i is the grid variation index, and Δ is a box side length.

Grid type	i	δ (km)	$\min \Delta = n\delta$	$\max \Delta = n\delta$	Total area (km ²)	Area of fine resolution (km ²)
Constant:15	—	15.0	15 km, $n=1$	—	(900) ²	all
2-Step:15	10	15.0	15 km, $n=1$	30.0 km, $n=2$	(900) ²	(300) ²
Graded:10	2	2.5	10 km, $n=4$	32.5 km, $n=13$	(910) ²	(100) ²
Graded:15	2	2.5	15 km, $n=6$	32.5 km, $n=13$	(910) ²	(210) ²

Grid type	Total number of boxes (points)	Percent of the Constant:15 total	Number of boxes in the central (210 km) ² region
Constant:15	3,600	100	196
2-Step:15	1,200	33	196
Graded:10	1,396	39	276
Graded:15	1,316	37	196

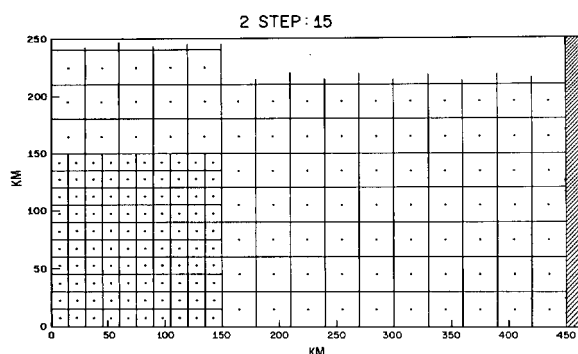


FIGURE 2.—A section of the northeast quadrant of the 2-Step:15 grid. The hatched area represents the boundary which encloses the entire (900 km)² region.

characteristics of the four grids used in the integrations. The constant-resolution mesh was used to generate comparison control cases for the variable-resolution cases. The 2-Step:15 “telescope”-type grid has a 20×20 fine-resolution interior mesh surrounded by a coarse mesh; a portion of the northeast quadrant of the grid is shown in figure 2. Figure 3 shows a similar section of the Graded:15 mesh, which has an interior 14×14 fine mesh with a (15 km)² box area. The central region of the Graded:10 mesh is depicted in figure 4. Here, the interior mesh is 10×10 and has a box area of (10 km)². The Graded:10 and Graded:15 grids differ in structure only within the (75 km)² central region; the grids are identical otherwise. From table 2, we also note the large percent-reduction of total number of grid points in going from the constant-resolution mesh to the variable-resolution grids. A summary of the graded grid construction follows:

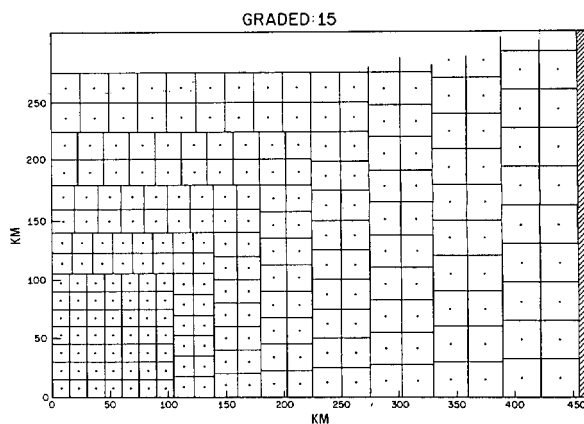


FIGURE 3.—A section of the northeast quadrant of the Graded:15 grid. The hatched area represents the boundary which encloses the entire (910 km)² region.

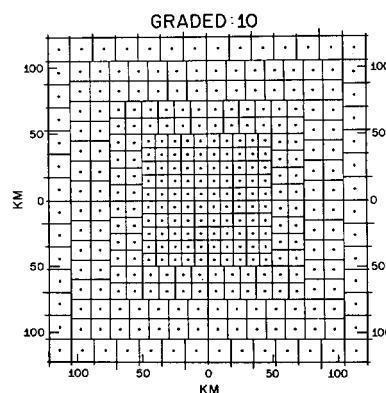


FIGURE 4.—The central region of the Graded:10 grid.

1. A basic side length δ is selected. This is the amount that box side length will increase in going outward from one annulus to the next.

2. The grid variation index i (a positive integer) is chosen. The initial core region will contain $(2i \times 2i)$ basic elements, and a square annulus will have i rings of equal-area boxes.

3. Let $n=1, 2, 3, \dots$ represent the count of the annuli interfaces. At the n th interface, the inner annulus is composed of boxes having side length $n\delta$, and the outer annulus of those with side length $(n+1)\delta$. There are $i(n+1)$ inner annulus boxes at the interface; adjacent to these are $i(n)$ outer annulus boxes.

4. The positive integer k is determined such that $k\delta = \Delta S_{min}$, where ΔS_{min} is the desired mesh length for the fine inner region grid. The annuli for $n=1, 2, \dots, (k-1)$ are deleted and replaced with a fixed-resolution mesh which has box side length $k\delta$.

3. THE PHYSICAL MODEL AND BOUNDARY CONDITIONS

The physical model adopted for the experiments was governed by the free-surface (shallow water) equations written in flux form on an f -plane in x, y rectangular Cartesian coordinates (x positive eastward, y positive

northward). The equations are

$$\frac{\partial h}{\partial t} = -\frac{\partial}{\partial x}(hu) - \frac{\partial}{\partial y}(hv), \quad (2a)$$

$$\frac{\partial hu}{\partial t} = -\frac{\partial}{\partial x}(huu) - \frac{\partial}{\partial y}(huv) + hf v - gh \frac{\partial h}{\partial x}, \quad (2b)$$

and

$$\frac{\partial hv}{\partial t} = -\frac{\partial}{\partial x}(huv) - \frac{\partial}{\partial y}(hvv) - hf u - gh \frac{\partial h}{\partial y}. \quad (2c)$$

Here, h is the height of the free surface, u is the eastward component of the horizontal velocity, v is the northward component of velocity, g is a constant gravitational acceleration, f is the constant Coriolis parameter, and t is time. The fluid is contained in a square basin which has a plane level bottom.

Two sets of boundary conditions were used in the experiments. In one set the physical system is closed; that is, the fluid is bounded by fixed vertical walls. Here, the no-normal transport, free-slip conditions hold and the height of the free surface is allowed to change with time. In the second set, the east and west boundaries are open and the fluid is assumed to have cyclic continuity. The north and south boundary conditions are as before.

The mean total available energy (henceforth called total energy) of the fluid system at a time t is given by

$$\overline{TE} = \frac{1}{2\sigma} \int_{\sigma} [h(u^2 + v^2) + g(h - \bar{h})^2] d\sigma \quad (3)$$

where \bar{h} is the areal mean height of the fluid, and σ is the total area of the region under consideration. The percent change in total energy from that at the initial time $t=t_0$ is defined by

$$\Delta \overline{TE} = (\overline{TE} - \overline{TE}_0) / \overline{TE}_0. \quad (4)$$

$\Delta \overline{TE}$ was computed at every time step in all of the experiments. In the absence of numerical truncation and round-off error, $\Delta \overline{TE}$ is zero with either of the above sets of boundary conditions.

4. INITIAL CONDITIONS

Two sets of initial conditions were used in the numerical integrations:

1. An easterly jet under geostrophic balance, with the height and speed fields specified by

$$H(y) = \bar{H} - H \cos(\pi y / Y_N) \quad (5)$$

and

$$U(y) = -\frac{g \pi H}{f Y_N} \sin(\pi y / Y_N). \quad (6)$$

There is no x variation; y ranges in value from $y=0$ at the southern boundary to $y=Y_N$ at the northern boundary. H is a constant with the dimensions of height. Profiles of $H(y)$ and $U(y)$ are shown in figure 5. With the condition

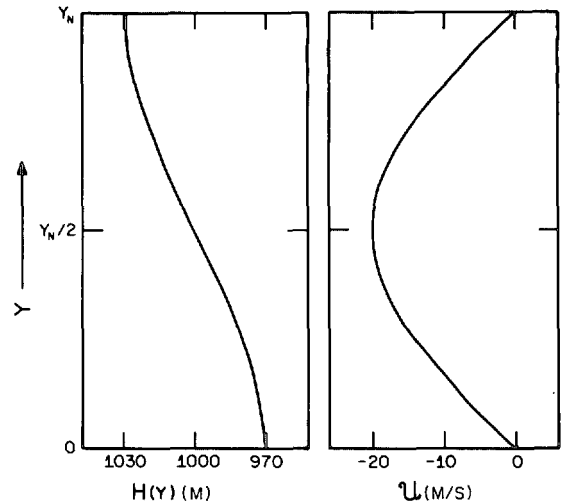


FIGURE 5.—Meridional profiles of the height and speed fields for the easterly jet initial condition.

that $U_{max} = -20.0$ m/s we have $H \approx 30.0$ m, which is the maximum departure of the fluid from the mean height \bar{H} .

2. A circular vortex in gradient balance, with the height field specified by

$$H(R) = \bar{H} + h \quad (7)$$

where

$$h = \begin{cases} -\hat{H} \cos^m \left[\frac{\pi}{2} (R/R_{max})^Q \right], & \text{for } R \leq R_{max} \\ 0, & \text{for } R > R_{max}. \end{cases}$$

In eq (7), \bar{H} is the height of the undisturbed fluid at distances far from the vortex center, \hat{H} is a constant with the dimensions of height, R is the radial distance from the geometric center of the vortex ($R^2 = x^2 + y^2$), R_{max} is the radial distance from the center of the system at which the vortex motion vanishes, m is a positive integer, and Q is a rational number. $Q=1/3$ and $R_{max}=405$ km were used in all of the experiments. Under the gradient balance assumption, the magnitude c of the fluid velocity is given by

$$c = \frac{-fR}{2} + \sqrt{\left(\frac{fR}{2}\right)^2 + gR \frac{\partial h}{\partial R}}. \quad (8)$$

The east-west and north-south velocity components are then given by

$$u = -c \sin \phi$$

and

$$v = c \cos \phi$$

where $\phi = \tan^{-1}(y/x)$. Figure 6 shows radial profiles of h and c for various values of the parameters \hat{H} and m which were used in the computations.

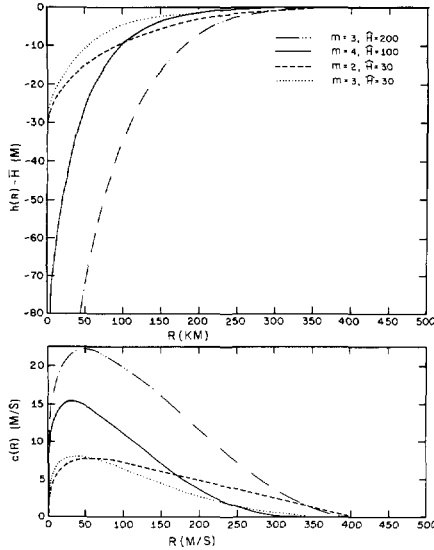


FIGURE 6.—Radial profiles of the height departure and magnitude of the fluid velocity for the balanced-vortex initial condition.

The numerical values of the functions were computed for the first (northeast) quadrant only, and assigned to the remaining three quadrants under the symmetry conditions of the system.

5. FINITE-DIFFERENCE EQUATIONS

Equations (2a, 2b, 2c) are transformed to the discrete form of area-integral equations by methods described in detail by Noh (1964). This technique was used by Kurihara and Holloway (1967) in a global primitive equation model, with some success. A brief description of the method follows. If σ is an arbitrary element of area, then for any scalar α we can write the integral equation

$$\int_{\sigma} \left(\frac{\partial \alpha}{\partial t} + \nabla_H \cdot \alpha \mathbf{V}_H + B \right) dS = 0 \quad (10)$$

as

$$\frac{\partial \bar{\alpha}}{\partial t} \Delta S_{\sigma} + \oint_C v_n \alpha dl + \bar{B} \Delta S_{\sigma} = 0 \quad (11)$$

where $(\bar{})$ is the mean value over the element σ and ΔS_{σ} is the area of σ . B is either a source term for α or an external force. $\nabla_H \cdot$ is the horizontal divergence operator, v_n is the outward normal component of the horizontal velocity vector \mathbf{V}_H , and C is the boundary contour of the area element σ . In our experiments all elements are rectangles, hence the line integral in eq (11) can be written as

$$\oint_C v_n \alpha dl = \int_{x_1}^{x_2} [(-\alpha v)_{y=y_1} - (-\alpha v)_{y=y_2}] dx + \int_{y_1}^{y_2} [(\alpha u)_{x=x_2} - (\alpha u)_{x=x_1}] dy \quad (12)$$

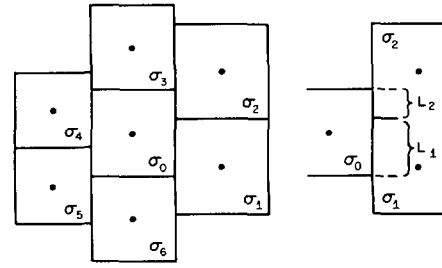


FIGURE 7.—A typical box configuration. In the text, the area integral is being evaluated over the box σ_0 . L_1 is the length of the line segment common to the boxes σ_0 and σ_1 , and L_2 is the length of the segment common to σ_0 and σ_2 .

where the x_i and y_j are the x, y coordinates of the vertices of the rectangle. These integrals are evaluated by assuming that the integrands are given on the line segments (box sides) by the mean values of the variables from adjoining boxes which have a common side. In the following, we will use operator notation similar to that of Kurihara and Holloway (1967). See section 2 of their paper for a complete discussion of the operators' characteristics. In their notation,

$$\oint_C v_n \alpha dl \approx N(Z) \Delta S_{\sigma} \quad (13)$$

where α is given by $\alpha = hZ$, with Z an arbitrary scalar, and

$$N(Z) = \left(\sum_E - \sum_W \right) \left[\frac{(hu)_0 + (hu)_i}{2} Z w_i \right] + \left(\sum_N - \sum_S \right) \left[\frac{(hv)_0 + (hv)_i}{2} Z w_i \right] \quad (14)$$

Here, the summations are over the l boxes which are contiguous to the box $\sigma = \sigma_0$; E, W, N, and S represent the east, west, north, and south sides of the boxes which all have their sides oriented in the cardinal directions, and $w_i = L_i / \Delta S_{\sigma_0}$ where L_i is the length of the line segment common to σ_0 and σ_i . Figure 7 shows a typical box configuration.

In the momentum equations, the Coriolis terms are given by

$$f(\bar{h}v) \Delta S_{\sigma} \quad (15a)$$

and

$$f(\bar{h}u) \Delta S_{\sigma} \quad (15b)$$

since f is a constant in the experiments.

Of final concern are the integral forms of the pressure gradient terms

$$g \int_{\sigma} h \frac{\partial h}{\partial x} dS \quad (16a)$$

and

$$g \int_{\sigma} h \frac{\partial h}{\partial y} dS. \quad (16b)$$

Two distinct numerical forms arise from the application of simple cubature rules in evaluating the integrals

(16a, 16b) over rectangular regions. One method of evaluation yields

$$g \int_{\sigma} h \frac{\partial h}{\partial x} dS \approx \frac{g \Delta S_{\sigma}}{4} \left[\left(\sum_E - \sum_W \right) w_i (h_i^2 - h_0^2) \right] \\ = g \Delta S_{\sigma} L_x(h, h) \quad (17a)$$

and

$$g \int_{\sigma} h \frac{\partial h}{\partial y} dS \approx \frac{g \Delta S_{\sigma}}{4} \left[\left(\sum_N - \sum_S \right) w_i (h_i^2 - h_0^2) \right] \\ = g \Delta S_{\sigma} L_y(h, h). \quad (17b)$$

A second method gives

$$\frac{g}{2} \int_{\sigma} \frac{\partial h^2}{\partial x} dS \approx \frac{g}{2} \frac{\Delta S_{\sigma}}{4} \left[\left(\sum_E - \sum_W \right) w_i (h_i + h_0)^2 \right] \\ = \frac{g}{2} \Delta S_{\sigma} G_x(hh) \quad (18a)$$

and

$$\frac{g}{2} \int_{\sigma} \frac{\partial h^2}{\partial y} dS \approx \frac{g}{2} \frac{\Delta S_{\sigma}}{4} \left[\left(\sum_N - \sum_S \right) w_i (h_i + h_0)^2 \right] \\ = \frac{g}{2} \Delta S_{\sigma} G_y(hh). \quad (18b)$$

$G_S(\)$ and $L_S(\)$ (where S is either x or y) are the operator notations of Kurihara and Holloway (1967). In these expressions the summation convention is the same as that for eq (14).

The equations for the time changes of the areal averages (over σ_0) of the dependent variables, which are the analogs of eq (2a, 2b, 2c) are (at time $t = n\Delta t$, n a positive integer):

$$\frac{\partial h_0}{\partial t} = -N^n(1), \quad (19a)$$

$$\frac{\partial (hu)_0}{\partial t} = -N^n \left(\frac{u_0 + u_i}{2} \right) + f(hv)_0^n - g \left\{ \frac{\frac{1}{2} G_x^n(hh)}{L_x^n(h, h)} \right\}, \quad (19b)$$

and

$$\frac{\partial (hv)_0}{\partial t} = -N^n \left(\frac{v_0 + v_i}{2} \right) - f(hu)_0^n - g \left\{ \frac{\frac{1}{2} G_y^n(hh)}{L_y^n(h, h)} \right\}. \quad (19c)$$

Here, either the $G_S(\)$ or $L_S(\)$ operator is to be used as the representation of the pressure gradient terms, and the box index subscript replaces the overbar notation for the mean value.

It can be shown that this system of equations conserves mass and quadratically conserves momentum. The total energy [eq (3)] of the system is not conserved because of the design of the $G_S(\)$ and $L_S(\)$ operators.

The time differences are written in the familiar centered-difference "leapfrog" form. All integrations were initiated with a forward time-difference set of equations.

For a constant (equal area) box subdivision of the integration domain, eq (19a, 19b, 19c) reduce to equations

which can be written in terms of the mean and difference operators

$$\bar{\alpha} = \frac{1}{2} \left[\alpha \left(x + \frac{\Delta}{2} \right) + \alpha \left(x - \frac{\Delta}{2} \right) \right] \quad (20a)$$

and

$$\alpha_x = \frac{1}{\Delta} \left[\alpha \left(x + \frac{\Delta}{2} \right) - \alpha \left(x - \frac{\Delta}{2} \right) \right]. \quad (20b)$$

With this notation, the equations for a fixed-resolution mesh are

$$\bar{h}_i + (\overline{hu})_x + (\overline{hv})_y = 0, \quad (21a)$$

$$(\overline{hu})_i + (\overline{hu})_{x-x} + (\overline{hv})_{y-y} - fhv + g \left\{ \frac{\frac{1}{2} [\frac{1}{2} (\overline{h^2})_x + h\bar{h}_x]}{\frac{1}{2} (\overline{h^2})_x} \right\} = 0, \quad (21b)$$

and

$$(\overline{hv})_i + (\overline{hu})_{x-x} + (\overline{hv})_{y-y} + fhu + g \left\{ \frac{\frac{1}{2} [\frac{1}{2} (\overline{h^2})_y + h\bar{h}_y]}{\frac{1}{2} (\overline{h^2})_y} \right\} = 0. \quad (21c)$$

Here, we note that the equations are very nearly in total energy conservation form (see Grammelvedt 1969, scheme B) except for the height gradient terms. The term $\frac{1}{2} (\overline{h^2})_s = L_s(h, h)$ which appears in both formulations of the momentum equations prevents the energy conservation property.

The no-normal transport boundary condition is numerically applied by making appropriate modifications to the operator $N(Z)$ [eq (14)] for the boxes adjacent to the walls. Here, the arithmetic mean which represents the normal transport at the wall is set equal to zero. The free-slip condition is computationally unnecessary in this formulation; in fact, viscous effects would have to be explicitly represented by a source term in the numerical equation if they were present at the wall, which is not the case here.

Although a physical boundary condition for the height of the free surface is not necessary, the difference equations require this knowledge for the numerical evaluation of the $G_S(\)$ and $L_S(\)$ operators. Here, the height of the surface at the wall (which is allowed to vary with time) is assumed to have the value of h for the box adjacent to the wall. This is equivalent to numerical evaluation by the method of images of the boundary condition $\bar{n} \cdot \nabla h = 0$. The above assumption allows us to avoid extrapolations in evaluating the height field at the fixed wall.

The finite summation analog of eq (3) is given by

$$\overline{TE} = \sum_k \sum_j TE_{j,k} \Delta S_{j,k} / \sigma \quad (22)$$

where

$$TE_{j,k} = \frac{1}{2} (u_{j,k}^2 + v_{j,k}^2) h_{j,k} + \frac{g}{2} (h_{j,k} - \bar{h})^2 \quad (23)$$

TABLE 3.—List of the numerical integration experiments. EJ is the easterly jet initial state; BV(m, \hat{H}) is the balanced vortex initial state for the parameters m and \hat{H} ; L and G are the operators $L_S(\)$ and $G_S(\)$ respectively; CB represents the closed boundary condition, and CC represents the east-west cyclic continuity boundary condition.

Experiment group	Experiment number	Initial state	Grid type	Δt (s)	Number of iterations	Gradient operator	Initial data	Boundary condition
A	1	EJ	2-Step:15	90	100	L	\overline{hu}	CC
	2	EJ	2-Step:15	90	100	L	\overline{hu}	CC
	3	EJ	2-Step:15	90	100	G	\overline{hu}	CC
	4	EJ	2-Step:15	90	960	G	\overline{hu}	CC
	5	EJ	2-Step:15	90	960	G	hu	CC
	6	EJ	Graded:15	90	960	G	hu	CC
	7	BV(2,30)	2-Step:15	90	960	G	hu	CC
	8	BV(2,30)	Graded:15	90	960	G	hu	CC
	9	BV(2,30)	2-Step:15	90	1,920	G	hu	CB
B	10	BV(3,30)	Constant:15	90	1,920	G	hu	CB
	11	BV(3,30)	2-Step:15	90	3,112	G	hu	CB
	12	BV(3,30)	Graded:10	60	2,880	G	hu	CB
	13	BV(3,30)	Graded:15	90	1,920	G	hu	CB
C	14	BV(4,100)	Constant:15	90	1,920	G	hu	CB
	15	BV(4,100)	2-Step:15	90	1,920	G	hu	CB
	16	BV(4,100)	Graded:10	60	2,880	G	hu	CB
	17	BV(4,100)	Graded:15	90	1,920	G	hu	CB
Off-center	18	BV(4,100)	Constant:15	90	1,920	G	hu	CB
D	19	BV(3,200)	Constant:15	90	4,998	G	hu	CB
	20	BV(3,200)	2-Step:15	90	3,404	G	hu	CB
	21	BV(3,200)	Graded:15	90	4,551	G	hu	CB

is taken as the average value of the total energy of the fluid in the j th box of the k th annulus. $\Delta S_{j,k}$ is the area of the box, σ is the total area of the region under consideration, and \bar{h} is the mean height of the free surface over σ .²

For the Graded:15 grid experiments, eq (22) was written as

$$\overline{TE} = \frac{1}{132,496} \sum_{k=6}^{13} k^2 \sum_{j=1}^{N_k} TE_{j,k} \quad (24)$$

where $TE_{j,k}$ has the definition given by eq (23). In this case, $\Delta S_{j,k} = (k\delta)^2 \text{ km}^2$, the number of boxes, N_k , in the k th annulus is $N_k = 16k$ for $k \geq 7$, and $N_6 = 196$ (since $k=6$ represents the 14×14 interior fine mesh). The Graded:10 grid formula for \overline{TE} is analogous to eq (24). Equation (22) reduces to simple summation formulas for the Constant:15 and 2-Step:15 experiments.

Similar formulas for computing the mean value of the square of the v -component, v^2 , were used in several of the experiments.

6. THE EXPERIMENTS AND RESULTS

Table 3 lists the experiments that are discussed in this paper. Of these, we present detailed results for the groups A, B, C, and D, since they provide the main basis for determining the relative merits of the various grid systems.³

² After 2,000 iterations, \bar{h} decreases by approximately two parts in 10^{12} , which indicates that the leapfrog time-integration scheme is slightly dissipative.

³ The remaining experiments are discussed in the appendix. All computations were performed on a Control Data Corporation 6600 computing system.

Experiments 10 through 13 were computed using four different grids with the same weak vortex as the initial state. Experiments 14 through 17 repeated those above except that the initial state was a more intense vortex (fig. 6). In all these cases, the initial vortex was specified so that its center coincided with the geometric center of the grid. On the other hand, experiment 18, which is comparable to experiment 14, had the center of the initial vortex displaced $7.5\sqrt{2}$ km to the northeast of the geometric center of the grid.

A very intense vortex (fig. 6) was specified as the initial condition for experiments 19, 20, and 21. Here, the three grids with a $(15 \text{ km})^2$ interior box were used, and the integrations were continued out in time until the calculations showed that the system was computationally unstable (the criterion was that the total energy increase by 50 percent over the initial value).

The following values of parameters were used in all the experiments:

$$f = 5 \times 10^{-5} \text{ s}^{-1},$$

$$\bar{H} = 1000 \text{ m},$$

and

$$g = 9.8 \text{ m/s}^2.$$

THE EASTERLY JET EXPERIMENTS

Group A. Since the analytic system of equations with the specification of easterly jet initial conditions and appropriate boundary conditions yields a steady-state solution, the behavior of the errors introduced by the finite-difference approximation to the initial conditions

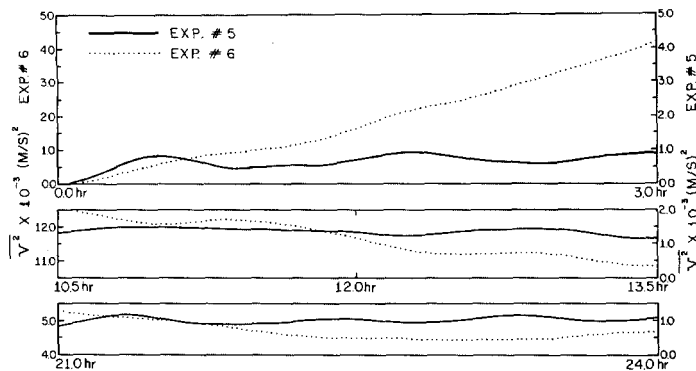


FIGURE 8.—Time variation of \bar{v}^2 for the experiments in group A. Note the change in ordinate scales.

is a measure of the error induced by the mesh. These approximations are not in geostrophic balance since both the height and fluid velocity fields were analytically specified. Figure 8 shows the temporal variation of \bar{v}^2 , which is zero analytically but finite nonzero in the integrations because of the above-mentioned errors. Three 3-hr periods are depicted from the 24-hr forecast period for both experiment 5 and experiment 6. In experiment 5 we note that after an initial growth of \bar{v}^2 , by 12 hr the computations become stable (bounded), and \bar{v}^2 exhibits a slow (~ 1 hr) oscillation with time. In contrast, experiment 6 shows a growth of \bar{v}^2 to values which are an order of magnitude larger than that of experiment 5. Here, \bar{v}^2 reaches a maximum ($12.7 \times 10^{-3} \text{ m}^2 \text{ s}^{-2}$) at about 10 hr and begins to decrease with time. After 22 hr, the graph exhibits a slow, bounded oscillation with values approximately five times larger than those of experiment 5. The traces of $\Delta \overline{TE}$ (not shown) exhibit a similar behavior, with the experiment 6 trace having larger amplitude than that for experiment 5.

After 24 hr, the v -component fields (not shown) in both experiments show a two-space increment ($2\Delta S$) noise pattern evenly distributed over the entire region of integration. (This is also true for the height fields, with the maximum variation being less than 1 m.) Of interest is the fact that over the 12×12 equal-interval fine mesh which is common to both grids, $\bar{v}^2 = 0.00462$ for experiment 5 and $\bar{v}^2 = 0.00205$ for experiment 6. This is opposite to the result for the entire regime and indicates that, for fluid motions with moderate shear in the mass and momentum fields, the graded grid structure induces relatively large errors of alternate sign throughout the annuli structure. However, the central region yields a state of less error as the computations stabilize.

A detailed examination of the initial tendency patterns for both experiments revealed that the errors in the tendencies computed at the inner interface boxes in the 2-Step:15 case were at times two orders of magnitude larger than those for the Graded:15 case. This helps explain the paradoxical behavior of the \bar{v}^2 statistics previously mentioned. Although the errors forced by the interface of the 2-Step:15 grid are relatively large, the cumulative effect of the errors induced by the graded grid over a much larger portion of the integration region is a larger value of \bar{v}^2 . This is also true of the $\Delta \overline{TE}$ computa-

tions. After 960 iterations, the innermost region (12×12 central mesh) of the graded grid had less error than the equivalent portion of the 2-Step grid; that is, the amplitude of the induced gravity wave structure was larger in the latter case. This can be attributed to the abrupt change in grid size at the interface of the coarse- and fine-mesh regions. In general, though, the 2-Step type structure gives a better overall representation of the variable states than a graded structure in cases where there are non-negligible shears in the velocity and height fields in the nonuniform portions of the grid.

THE BALANCED-VORTEX EXPERIMENTS

In the following discussion, the root-mean-square error of the height field (denoted by RMSE:h) is used as a comparative statistic. The data are taken from the $(210)^2 \text{ km}^2$ central square region which is common to the four grids and contains the most active portion of the vortex. The comparison is with the data from the initial time t_0 .

After the initial time step, the error in the height and velocity component fields results from a combination of

1. space-differencing truncation,
2. forward time-extrapolation,
3. approximation of the areal mean values of the dependent variables by point values, and
4. imbalance of the discrete system caused by specifying both the height and velocity component fields analytically.

Group B. The initial state for these experiments was a centered balanced vortex having a height deficit of 30 m at the center and a speed maximum of about 8 m/s near 40 km from the center.

Within the first 100 iterations, the computations for all four experiments reached quasi-equilibrium (slowly varying) balanced states as they recovered from the imbalances induced by the initial finite-difference representations. Figure 9 shows the percent change in total energy and RMSE:h for the 3-hr period ending at 48 hr. The traces for the preceding hours of the forecast are not presented because of their similarity to those shown.

Of all the profiles of $\Delta \overline{TE}$, the Graded:15 case shows the most active variation, with a pronounced two time-increment ($2\Delta t$) oscillation. Otherwise, all four profiles are remarkably similar in that the traces show no apparent trend and are upper bounded by the 0.01 percent change isoline. The RMSE:h profiles have the same trend and boundedness character as the $\Delta \overline{TE}$ profiles except that here we do see the effect of the variable-resolution mesh on the computations. The control computation (exp. 10) has an average height error which is generally less than 0.5 m, whereas the other experiments have average height errors between 0.75 and 1.25 m. Each of the curves exhibits a $4\Delta t$ – $6\Delta t$ oscillation which is probably directly related to the gravity wave motion on the free surface. Considering the energy and mean height changes together for each case, we note that the Graded:10 results are slightly better than the comparable 2-Step:15 results and both of these are only slightly better than the Graded:15 results. In terms of computational expediency, the 2-Step grid would be preferred. Experiment 11 was continued out to 77.8 hr.

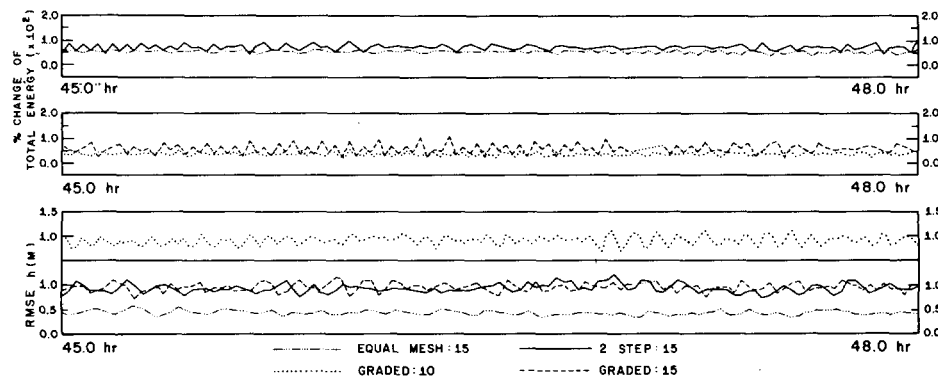


FIGURE 9.—Percent change in total energy, $\Delta \overline{TE}$, and root-mean-square error of the height field, RMSE:h, for the experiments in group B (Equal Mesh:15=Constant:15).

The profiles are similar to those shown; the percent change in total energy remains less than 0.01 percent.

Group C. The initial state for these experiments was a more intense vortex than that used for group B. The central height deficit was 100 m (10 percent of the undisturbed fluid height) and the maximum tangential speed was 15.5 m/s near 30 km from the center (fig. 6). Figure 10 shows RMSE:h for five 3-hr intervals during the 48-hr forecast period. We note that the large error during the initial iterations diminishes (stabilizes) rapidly in the equal-mesh case (exp. 14). For this case, throughout most of the forecast, RMSE:h remains in the range 1.0–1.25 m and oscillates with a period of about 9 min. In the other cases, the error is about twice that magnitude and the oscillations have larger amplitudes with variable periods of from 4 to 9 min. Of the three variable grids, the Graded:10 (exp. 16) gives a slightly better height field for the first 24 hr, but the three profiles are comparable at 36 hr, with the Graded:15 and 2-Step:15 experiments having slightly better results at 48 hr. The profiles of $\Delta \overline{TE}$ (fig. 11) for the 3-hr periods corresponding to those

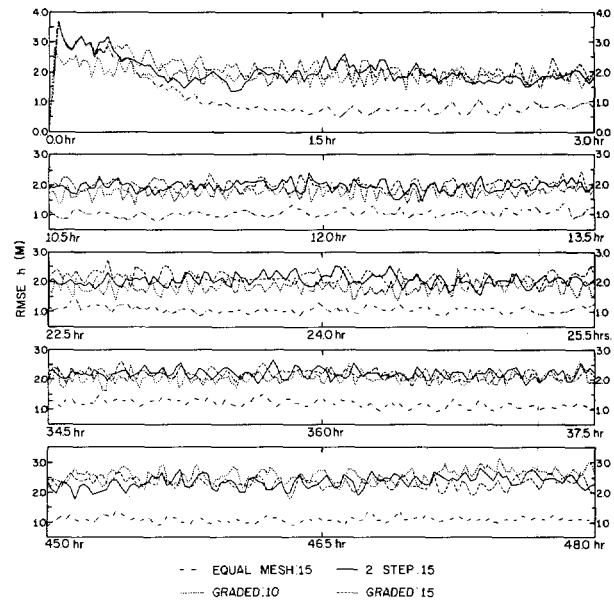


FIGURE 10.—Root-mean-square error of the height field, RMSE:h, for the experiments in group C (Equal Mesh:15=Constant:15).

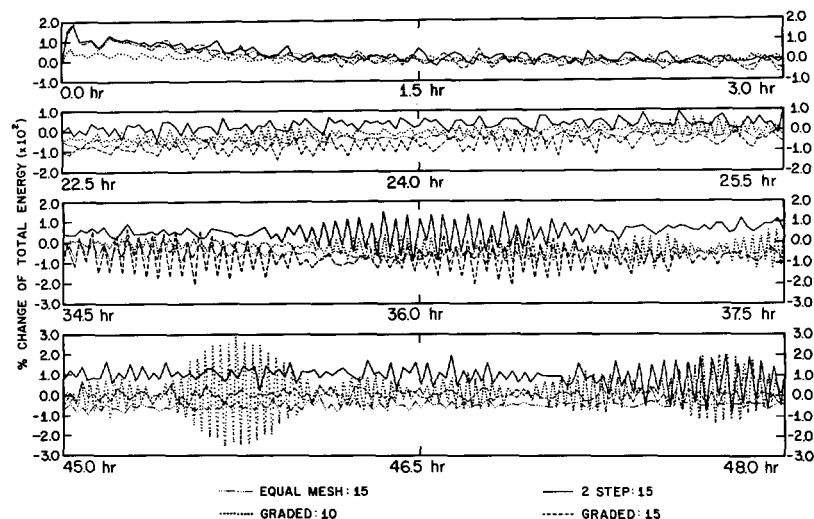


FIGURE 11.—Percent change of total energy $\Delta \overline{TE}$ for the experiments in group C (Equal Mesh:15=Constant:15).

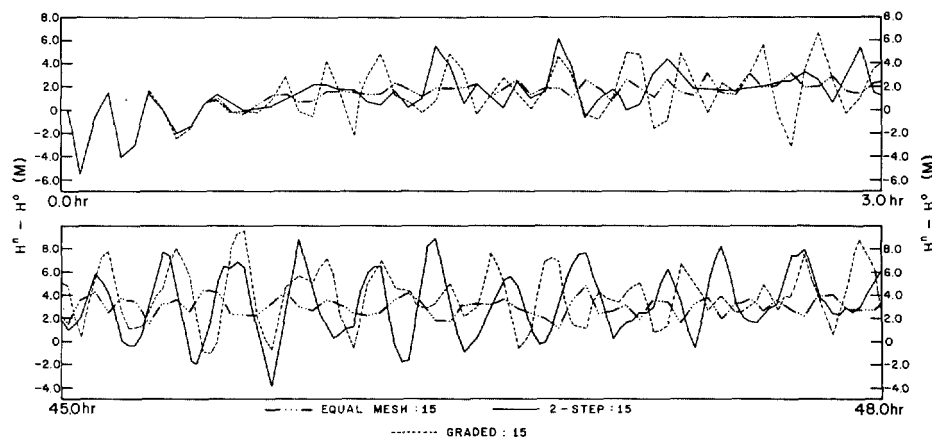


FIGURE 12.—Departures from the initial height H^0 of the fluid in one of the four central boxes for experiments 14, 15, and 17. H^n is the height of the fluid at time $n\Delta t$ (Equal Mesh:15=Constant:15).

of $RMSE:h$ give further insight into the behavior of the computations. Initially, all four profiles of ΔTE have the same character except that the 2-Step:15 and Graded:15 curves exhibit slightly larger amplitudes. The profiles for experiments 15, 16, and 17 have trends which indicate very slow increases in total energy. In the 3-hr period centered at 24 hr, all experiments show a tendency for a $2\Delta t$ oscillation in the profiles which is most pronounced in the Graded:10 and Graded:15 cases. The Graded:10 amplitudes are modulated, with maximum amplitude occurring at about 50-min intervals. The 2-Step:15 and Graded:15 cases exhibit the largest percentage changes.

The next period shown (centered at 36 hr) has profiles which have a pronounced $2\Delta t$ oscillation for all the experiments in this group. Again, the amplitudes are largest in the Graded:15 and 2-Step:15 cases. The amplitudes for the variable grid cases are modulated, the 2-Step:15 with a period of approximately 120 min, the Graded:15 of about 90 min, and the Graded:10 of about 35 min. The Graded:10 profile is beginning to show changes which indicate that the computations are becoming less stable.

At 45–48 hr, the control experiment has a relatively steady profile with an average percentage change of about -0.005 . Of the three variable-grid experiments, the Graded:15 computations give energy changes which most nearly resemble the control case in both magnitude and variation; the amplitude of the oscillations is less than that of the later periods previously examined, and the profile displays little change from the initial values. In contrast, the 2-Step:15 and Graded:10 experiments both exhibit total energy changes of variable amplitudes which are from four to six times larger than that for experiment 17. The Graded:10 profile continues to show a marked variable modulation of the $2\Delta t$ oscillation with an average period of about 35 min. The variation in amplitude has changed considerably from the earlier periods, the changes being by a factor of two to four. In the above experiments, the pronounced $2\Delta t$ oscillation in ΔTE can

be directly related to the behavior of the kinetic energy changes. The changes of mean available potential energy have relatively smooth oscillations of a longer period. Also, the final periods of the 2-Step:15 and Graded:10 forecasts have velocity component RMSE's (not shown) which have a slight $2\Delta t$ oscillation. The above symptoms strongly suggest that the computational noise is predominant in the velocity component fields.

Figure 12 shows the departure from initial height of the fluid in one of the four central boxes of the grid for the initial and last 3-hr period of the forecast. In all cases, these four boxes have equal height values throughout the forecast period. Only the experiments which used a $(15 \text{ km})^2$ interior box are shown. The initial displacements in all cases are a result of the initialization (finite differencing) errors and can be thought of as an impulse which initiates free oscillations in the systems. The effects of grid variation become apparent after about 20 min with gravity wave interactions causing changes in amplitudes and periods of the oscillation. In all cases the period was about $6\Delta t$ initially; the equal-mesh profile retains this period throughout the forecast but the profiles are modified in the other cases to those with somewhat longer and variable periods. These modifications are undoubtedly due to the differences in the behavior of the computational gravity waves which are generated by the variable-mesh differencing. The amplitude of the control case profile remains steady after the system reaches an equilibrium state but the other amplitudes show increases which probably result from the superposition of the additional gravity waves mentioned above. The Graded:15 and 2-Step:15 profiles are very similar, both having an average variation about four times that of the control case. Plan views of the velocity component and height fields (not shown) display symmetries throughout the entire forecast period. The u, v fields have radial (rotational 180°) anti-symmetry, and the h field has rotational (90°) symmetry. Detailed time-step examinations of the fields showed that there was apparently no time splitting of the fields; but

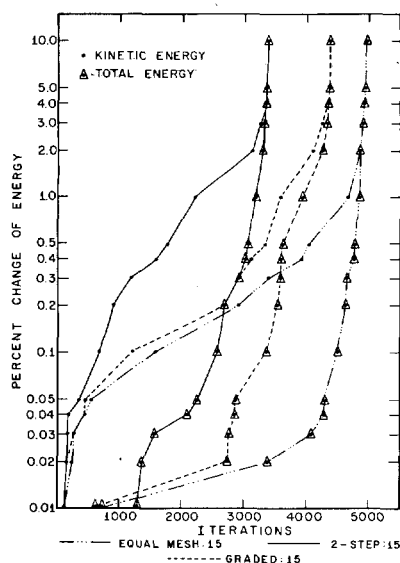


FIGURE 13.—Time iteration number of the first occurrence of certain percent changes of kinetic and total energy for the experiments in group D (Equal Mesh:15=Constant:15).

that the computations did produce $2\Delta S$ waves of small amplitude which were more evident in the control-case computations.

The effects of nonsymmetry are apparent in the results (not shown) for experiment 18 where the symmetric initial state was prescribed off-center in the grid system. Here, the gravity waves reflected at the boundaries at different times and the wave interaction pattern quickly destroyed the symmetry of the various fields. The center of the system remained in the box where it was initially prescribed, but its position is not stationary as evidenced by the oscillations in the mean velocity component values for this box. After 42 hr, a $2\Delta t$ oscillation became evident in both the percentage changes in kinetic energy and available potential energy, with the percentage changes in total energy increasing to an order of magnitude larger than those in the comparable centered-vortex experiment (exp. 14). The RMSE profile for the height field (not shown) has the same character as that of experiment 14.

Group D. The very intense vortex specified for this group of experiments gave a central height deficit of 200 m and a speed maximum of 22.1 m/s at 50 km from the center (fig. 6). With this specification the initialization errors are of much larger amplitude than those for groups B and C, and amplification of the computational errors through nonlinear interactions proceeds at a more rapid rate than for those experiments.

The profiles of ΔTE and $RMSE:h$ (not shown) have relatively the same character as those for the group C experiments (figs. 10 and 11) except that increases in amplitudes are in evidence earlier in the forecast period. In the later periods of the integrations, there is a pro-

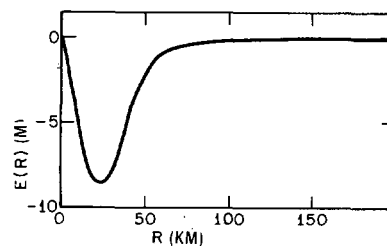


FIGURE 14.—The approximate form of the amplitude of the initial height error pattern for experiments 14 through 18.

nounced $2\Delta t$ oscillation in the ΔTE and kinetic energy profiles for each experiment.

Figure 13 gives the iteration count of the first occurrence of selected percentage changes (from the initial values) of kinetic and total energy. The 2-Step:15 grid computations reached all percentage change levels (greater than 0.02 percent) in the least number of iterations, the Constant:15 computations in the largest number, and the Graded:15 somewhat half-way between the two. All three experiments showed changes of up to 0.05 percent in kinetic energy during the initial 550 iterations, followed by moderate increases in the 2-Step:15 computations and relatively slow increases in the other two cases.

In these experiments, the velocity component and height fields showed symmetries similar to those described for the group C experiments throughout most of the forecast period. During the later iterations, noticeable asymmetries appeared in these fields, and as the computations approached instability, the symmetry in the fields was totally destroyed.

Discussion of the group B, C, and D results. The initial error pattern in the height field has a wave form given approximately by

$$E(R) \sin 4\theta, \quad 0 \leq \theta \leq 2\pi$$

where θ is the usual horizontal azimuth displacement. $E(R)$ is given schematically in figure 14, for experiments 14 through 18. This initial fluid displacement from the balanced state excites gravity wave propagation which is both radial and tangential; the tangential propagation being due, in part, to advection by the vortex fluid motion.⁴

The total height-field contour pattern is altered from the initial concentric circles to concentric elliptical shapes, and the contours retain this characteristic throughout the forecast periods regardless of the mesh on which the integration is performed. Wave reflection at the boundaries and subsequent wave interaction give rise to further error components because of the nonlinearity of the system.

In the variable-grid experiments, the mesh variation adds its error contribution through the advection of large grid-scale truncation by the gravity waves which reflect

⁴ In the equal-mesh computations (exp. 14) the initial impulse traveled radially to the boundary in 45 min ($30\Delta t$), which gives an average wave speed $c=165$ m/s.

from the boundaries. The truncation error is local in nature and initially dominates in the center of the grid system where the vortex is relatively intense. But here ΔS is minimum; hence, the maximum truncation error is equivalent to that for an equal-mesh system having the minimal grid increment. Within several tens of iterations, the excited truncation error of the coarser grid contaminates the computations on the fine sections of the grid; and all subsequent error analysis must use the largest mesh increment in an error estimate.

The above phenomenon is manifested in the profiles of $RMSE:h$ for the experiments, and therefore aids in a valid comparison of the integrations on the various grid systems. Certain aspects of the grid systems must be considered in the analysis. Referring to figures 2 and 3 and table 2, we note that the 2-Step:15 system has fixed fine resolution in the $(300 \text{ km})^2$ central region whereas that for the Graded:15 is in the $(210 \text{ km})^2$ central region. For the experiments in group B, this is relatively unimportant since the variations in the initial vortex height field and velocity components are small in the region from 105 km to 150 km from the center (fig. 6). The group C vortex (fig. 6) has a greater variation in this region. The Graded:10 system (fig. 4) improves the resolution of the vortex centers since the velocity component maxima are contained within the $(100 \text{ km})^2$ central region that has 10-km resolution. As was pointed out previously in the group B experiments, although the Graded:10 results were best relative to the control case, the comparable 2-Step:15 results indicate that the 2-Step:15 mesh would give sufficient resolution for weak vortex-type motions. The utility of the Graded:15 system was not realized here because of the weak character of the physical system in regions of grid variation; whereas the grid variation given by the Graded:10 system enhanced the representation of the vortex near its center. The truncation error generated in the coarse-mesh regions of the latter case was undoubtedly small because of the small amplitude of the gravity waves generated by the processes described previously.

The vortex prescribed in the group C experiments proved to be a more crucial test of the mesh systems. Clearly, for the first 24 hr of the forecast period, the Graded:10 variable grid yielded integrations which were superior to the other variable grid results; but by 36 hr the integrations on that grid gave results which were comparable to the 2-Step:15 and Graded:15 results. By 48 hr, this integration appeared to be degenerating under some form of computational instability. Detailed time-step examination of the height and velocity component fields revealed no time splitting of the fields as is usually observed in linear models which use the leapfrog time-integration scheme. But the large amplitude $2\Delta t$ oscillations of the ΔTE profile, when considered together with increasing values of $RMSE:h$, strongly suggest the presence of aliasing errors common to nonlinear systems that do not damp the large wave-number space oscillations. The

fact that the system remains stable may be a result of the inherent smoothing which is built into the "box" method of integration, but it appears that the computations are yielding to an accumulation of energy in the short wavelengths, and the physical system is deteriorating from a quasi-balanced state.

The $2\Delta t$ oscillation is evident in the ΔTE profiles for all the integrations in this group, including the control case. Hence, we might interpret this as a manifestation of an iteration-by-iteration "return to balance" phenomenon.⁵ The increase in amplitude of the ΔTE profiles for the variable-grid cases reflects the ability of the system to restore a balance under the influence of the errors generated at each time step.

Although the fine-resolution region of the 2-Step:15 grid contains a larger section of the vortex than does the analogous region of the Graded:15 grid, the results of the integration clearly demonstrate the advantage of a gradual change in mesh increment over an abrupt one. On each mesh there is essentially an increase in box area of 4 to 1 (table 2) going from the center of the system to the boundary. Figure 10 shows that there is no large difference in the $RMSE:h$ profiles for either case although there is an indication that the height field for the Graded:15 integration may be slightly better than that for the 2-Step:15 at the end of the 48-hr period. Table 4 lists the 3-hr time average of the $RMSE:h$ for the periods centered at 1.5, 24, and 46.5 hr. We note the obvious deterioration of the Graded:10 computations and the relative improvement of the Graded:15 computations over the 2-Step:15. The profiles of ΔTE for these cases show that there is indeed a difference in the character of the forecasts which is grid dependent.

The phenomena discussed above for the group C experiments are observed in the group D experiments except that they occur on a much shorter time scale. Here, the computational mode interacts nonlinearly with a large-amplitude physical mode and the computational noise grows at a rapid rate. The graph of energy changes versus iteration count for the control experiment 19 (fig. 13) shows the typical energy increases which are associated with the nonlinear computational instability of integrations done on a constant-resolution mesh. The additional

TABLE 4.—Three-hr time averages of $RMSE:h$ (m) for experiments 15, 16, and 17

Experiment number	Time periods (hr)		
	0-3	22.5-25.5	45-48
15	2.07	2.05	2.41
16	1.92	1.83	2.57
17	2.22	2.12	2.29

⁵ In the Graded:10 experiment (exp. 16), the modulated $2\Delta t$ oscillation in the ΔTE profile could possibly be interpreted as a "folding" of a temporal 2.1-2.2 increment oscillation in the manner described by Robert et al. (1970). The computational and/or physical significance of this frequency in the temporal variation of an areal average is not readily apparent.

computational noise introduced into the calculations by the use of a variable grid structure stimulates the growth of computational errors. This is evidenced by the graphs of energy changes for the 2-Step:15 and Graded:15 grid experiments (fig. 13).

In these experiments, kinetic energy is the principal component of the total energy; the available potential energy of the system is smaller by an order of magnitude. From the graphs (fig. 13) we note that the kinetic energy quickly undergoes relatively large percentage changes, but these are compensated for in the total energy change by very large percentage changes in available potential energy (not shown). Comparison of the results of the 2-Step:15 and Graded:15 grid computations against those for the Constant:15 grid shows that computational trends exhibited in the group C experiments were correctly interpreted. Here, the kinetic energy changes in the Graded:15 experiment closely resemble those of the control computation up to the 0.5 percentage change level, whereas those for the 2-Step:15 case differ noticeably. In the interval 0.05–0.5 percent, a percent change level was reached in the Graded:15 grid computations, on the average, in 85 percent of the number of iterations taken by the control case; whereas the average was 44 percent in the 2-Step:15 case.

A comparison of the percent changes of total energy shows that the number of iterations taken to reach a particular percent change level (in the interval 0.2–10.0 percent) was on the average 79 percent of the control case value for the Graded:15 grid case, whereas in the 2-Step:15 case the number was, on the average, 59 percent. These statistics certainly indicate that the error growth rate for computations done on the graded-type variable grid is substantially less than that for the comparable computations on a telescope-type grid.

7. SUMMARY AND CONCLUSIONS

Three variable Cartesian grids were used in the numerical integration of the shallow-water equations over a square two-dimensional domain. The grids were selected from a family of Cartesian grid structures which possesses many degrees of variation. The 2-step formulation has the advantage of having only one interface at which there is an abrupt change in mesh length, whereas the Graded:10 and Graded:15 systems of the double annulus group effect a gradual change. The single and triple annulus configurations (fig. 1) were not used since they gave variations which are either too pronounced or too gradual. For the experiments considered here, we restricted the inner to outer ring mesh ratios to be either 3:1 or 2:1.

Integrations on fixed fine-resolution mesh were done in three of the cases (groups B, C, D). These computations offer criteria against which the variable grid experiments can be compared. The differences in the results are due to the variation in mesh structure which (1) alters the

forms of the second order finite-difference equations in the regions of grid variations because of the box-method formulation and (2) introduces further approximation errors through an averaging process along the line segments which form the boundaries of the individual boxes. This essentially introduces spatial smoothing into the integration formulas. The equations do not conserve total energy, but the computations for the control (constant mesh) cases showed no apparent trend toward an increase or decrease of total energy throughout the forecast periods for experiments 10 and 14, and for most of the experiment 19 forecast. Hence, we can consider the finite-difference equations to be "nearly" total energy conserving. The weak vortex computations (group B) yielded total energy changes which closely approximated those of the control case.

In the computations with a more intense vortex (group C), the departures from the control case are pronounced in some instances but remain less than 0.03 percent in magnitude. The behavior of the height field is more striking; the control case $RMSE:h$ shows a bounded $6\Delta t$ oscillation (fig. 10) which is strongly correlated with the free oscillation at the vortex center (fig. 12), and which has a temporal mean of approximately 1.25 m. The variable-grid profiles of $RMSE:h$ have temporal means from two to three times larger with more pronounced variations. The group D experiments purposely used a very intense vortex as the initial state in order to observe the behavior of error growth and nonlinear computational instabilities. The results prior to the onset of instability replicate, on a shorter time scale, those of the group C experiments.

Although the differences in the results are due entirely to the grid structures, the amplification of some error is due to the nondamping characteristic of the time integration scheme. No effort was made to suppress the high-frequency temporal and/or spatial oscillations as might be done, say, with a Lax-Wendroff (1960) type integration rule; this is evident in the results for experiment 17.

Considering the experiments in toto, the results indicate that, for a *weak* vortex-type motion embedded in a zonal current, the 2-step type telescope grid might be adequate since the integrations have relatively small error. The computational times and computer memory requirements are minimal when compared to the comparable equal-mesh computations. On the other hand, for an *intense* vortex a graded-type grid yields relatively better numerical integrations at the expense of an increase in computational time (compared to that for the 2-step type grid). Clearly, though, relative to the constant resolution grid integrations, the graded-type variable grid yields integrations that are more satisfactory than the telescope-type grid in terms of both the error induced by the grid structure in the differencing schemes and the error growth rate.

The application of these horizontal grid structures to numerical integrations of primitive equation multilevel models of atmospheric systems can result in considerable

savings in computer memory requirements and running times. The graded annulus-type grids are systematically constructed and allow a large range of variation and resolution. For systems which are active in these central regions and quiescent in the peripheral regions, the central mesh can be specified to give resolutions that would permit definitions of small-scale phenomena. In these cases, the small time-increment needed to maintain computational stability would be a major consideration. For long-term integrations, such as in the study of hurricane dynamics, the growth of any computational mode (as evidenced in exp. 17) must be controlled since variable-type horizontal grid structures obviously generate error components that can become unstable if not damped. This instability is primarily due to nonlinear interaction. In these cases, a time integration scheme can be used that minimizes, or eliminates entirely, the computational mode. For model investigations of very short time-scale phenomena, such as cumulus dynamics, the damping of high-frequency oscillations might be unnecessary.

APPENDIX

Experiments 1, 2, 3, and 4 were designed to compare the height gradient operators $L_s(\)$ and $G_s(\)$. These experiments showed that the momentum tendencies and the v -component field had less error when the $G_s(\)$ operator was used. Hence, the $G_s(\)$ operator was used in all of the remaining experiments. Experiments 3, 4, and 5 differ only in the manner of specifying the initial values for the box-means of the dependent variables. In experiment 5, the point values of the functions [eq (5) and (6)] at the box centers were selected as the initial means. In experiments 3 and 4, initial values were specified through analytical integration of eq (5) and (6). A comparison of the results for these experiments showed that the correct mean values \overline{hu} , \overline{hv} , and \overline{h} gave slightly better results initially, but after several hundred iterations there were no significant differences in the $\overline{v^2}$ and $\Delta\overline{TE}$ statistics for these experiments. This indicated that the computational (finite difference) errors soon dominated the initialization errors in the calculations, and the point values hu , hv , and h were sufficient for beginning the integrations. The point values were used in the initialization of all subsequent experiments.

Experiments 7, 8, and 9 had a weak, flat profile vortex (fig. 6) for the initial state. East-west cyclic continuity was used in experiments 7 and 8; experiment 9 used a closed system. Comparisons of the experiments showed that, after an initial adjustment, the changes in mean total energy from the initial value for each experiment exhibited a smooth oscillation with time; but the amplitude of this oscillation in experiments 7 and 8 was $\sim 10^2$ kJ m $^{-2}$ whereas for experiment 9 it was $\sim 10^{-1}$ kJ m $^{-2}$ (the mean total energy \overline{TE} is on the order of 10^4 kJ m $^{-2}$ in these experiments). This behavior is related to the gravity wave interactions and the symmetry of the calculations. In the closed system, the initial perturbations on the prescribed height field (which are due to the differencing of the analytically specified initial fields) are symmetric and remain so throughout the entire integration. By removing the east and west walls and thereby allowing wave propagation through the system (instead of wave reflections at the walls), the symmetry patterns are altered; a strong beat pattern is induced and the north-south symmetry is strongly modified. The remaining experiments (10 through 18) were performed with the closed system to avoid this effect.

REFERENCES

- Anthes, Richard Allen, "Numerical Experiments With a Two-Dimensional Horizontal Variable Grid," *Monthly Weather Review*, Vol. 98, No. 11, Nov. 1970, pp. 810-822.
- Grammeltvedt, Arne, "A Survey of Finite-Difference Schemes for the Primitive Equations for a Barotropic Fluid," *Monthly Weather Review*, Vol. 97, No. 5, May 1969, pp. 384-404.
- Kurihara, Yoshio, and Holloway, J. Leith, Jr., "Numerical Integration of a Nine-Level Global Primitive Equations Model Formulated by the Box Method," *Monthly Weather Review*, Vol. 95, No. 8, Aug. 1967, pp. 509-530.
- Lax, Peter D., and Wendroff, Burton, "Systems of Conservation Laws," *Communications on Pure and Applied Mathematics*, Vol. 13, Interscience Publications, Inc., New York, N. Y., 1960, pp. 217-237.
- Noh, W. F., "CEL: A Time-Dependent Two-Space-Dimensional Coupled Eulerian-Lagrange Code," *Methods in Computational Physics*, Vol. 3, Academic Press, New York, N. Y., 1964, pp. 117-179.
- Robert, André J., Shuman, Frederick G., and Gerrity, Joseph P., Jr., "On Partial Difference Equations in Mathematical Physics," *Monthly Weather Review*, Vol. 98, No. 1, Jan. 1970, pp. 1-6.
- Shuman, Frederick G., and Stackpole, John D., "Note on the Formulation of Finite Difference Equations Incorporating a Map Scale Factor," *Monthly Weather Review*, Vol. 96, No. 3, Mar. 1968, pp. 157-161.

[Received November 30, 1970; revised February 8, 1971]